Batteries & Supercaps

Research Article
doi.org/10.1002/batt.202200132

Chemistry
Europe
European Chemical
Societies Publishing

www.batteries-supercaps.org

High Performance, Stoichiometric $ZnSnP_2$ Anode for Rechargeable Lithium-Ion Battery with Concomitant Conversion from Chalcopyrite to Sphalerite Phase

Shubham Patel[a] and Srinivasan Sampath*[a]

Herein, we report chalcopyrite phase of zinc tin phosphide ($ZnSnP_2$) as an anode for high rate, rechargeable, lithium-ion battery. In-situ Raman spectroscopy reveals the conversion of chalcopyrite phase of $ZnSnP_2$ to a symmetric sphalerite phase upon cycling, which helps in achieving stable and reversible capacity at high discharge rates. This is due to the low bandgap and high conductivity of the sphalerite phase. The in-situ phase conversion is extremely important as it is difficult to synthesize bulk $ZnSnP_2$ sphalerite phase by the known methods till date. After full phase conversion, a reversible capacity of 750 mAh g^{-1} is obtained towards the end of 1700 cycles at a rate of 5 A g^{-1}. Full cell assembled using $LiCoO_2$ as the cathode material yields a stable performance with a discharge capacity of around 500 mAh g^{-1} at 0.5 A g^{-1} and the rate capability studies demonstrate reversible capacities up to 15 A g^{-1} current.

Introduction

Lithium-ion batteries (LIBs) have been the first choice in electrochemical energy storage systems due to various advantages over other batteries. Small size of Li cation results in good transport properties and phase stability which help in fast charging, long cycle life and high power density.[1–4] Still, development of certain battery components is required to make this technology eco-friendly. For example, NMP is used as a solvent for fluorinated polymer-based binders during fabrication of the LIBs, which is toxic in nature and hard to recover.[5] Along with the solvent and binder, anode material is an important part of LIB and graphite-based anodes have been used for decades for the fabrication of commercial LIBs.[6] Graphite suffers due to its low theoretical capacity (372 mAh g^{-1}) and its mechanical degradation during electrochemical cycling.[7–9]

Apart from graphite, other group IVA elements and their alloys have been studied extensively as anode material for LIBs.[10] For example, Si, Ge, and Sn have attracted significant attention due to their extremely high theoretical capacities of 4200, 1624 and 994 mAh g^{-1}. Use of bulk elements as anode is limited due to high volumetric changes that occur during lithiation and de-lithiation cycles that lead to the development of cracks in the SEI layer upon cycling exposing fresh anode surface to the electrolyte solution leading to additional degradation.[11,12] For instance, SEI film formed on Sn foil anode has been shown to be unstable in ethylene carbonate (EC) based electrolytes which lead to its continuous reformation during cycling between 0.7 and 2.5 V.[13] Further, this leads to degradation of electrical contact between the material and current collector resulting in fast capacity fading and low coulombic efficiency.[14] Si and Ge based anodes have been explored to a great extent as compared to Sn-based ones, most probably due to their high theoretical capacity as compared to the latter. Certain attempts have been made to improve the performance of Sn-based anode materials.[15] For example, Cu_2ZnSnS_4 nanorods have been shown to deliver a capacity of 1360 mAh g^{-1} after 100 cycles, when cycled at low rates such as 0.2 A g^{-1}. At high rates of 0.5 A g^{-1}, capacity drops to around 500 mAh g^{-1}.[16] Certain intermetallic alloys such as SnSb:Fe/Co/Ni prepared by co-precipitation method also represent poor capacity retention of around 500 mAh g^{-1} at the end of 50 cycles.[17] More recently, Sn based nanomaterial supported on carbon nanotubes have been explored and long cycle life with a specific capacity of 560 mAh g^{-1} is obtained towards the end of 1000 cycles.[18] SnO_2/Sn nanoparticles supported on 2D carbon plates demonstrate relatively good performance as anode for LIB. The composite delivers high capacities of 815 and 560 mAh g^{-1} at the end of 400 and 800 cycles.[19]

In the present study, zinc tin phosphide ($ZnSnP_2$), a new Sn based anode which contains zinc (Zn) and phosphorous (P) as additional elements is explored as an anode for Li-ion battery. These elements can act as a buffer matrix and help in overcoming the problems associated with volume expansion of bulk Sn. Additionally, they may help in the enhancement of electrochemical conversion reaction for improved Li storage. The chalcopyrite $ZnSnP_2$, first reported in 1957 by Goodman[20] has been used as absorber for solar cells.[21–24] $ZnSnP_2$ is a p-type semiconductor which can exist in either chalcopyrite or sphalerite structure. The bandgap of chalcopyrite phase is around 1.70 eV whereas the sphalerite phase possesses a value of 1.30 eV. The ordered chalcopyrite phase crystallizes in tetragonal crystal system while the disordered sphalerite phase crystallizes in cubic crystal system. Cubic phase has been shown

[a] S. Patel, Prof. S. Sampath
Department of Inorganic and Physical Chemistry
Indian Institute of Science
Bangalore 560012, India
E-mail: sampath@iisc.ac.in

to deliver a stable performance as anode material because of high symmetry, which helps in achieving better stress accommodation.[25] Few other chalcopyrites such as $CuFeS_2$ and antimony based chalcopyrites have also been studied as anode materials for Li storage.[26,27] Discharge capacity of 870 mAh g^{-1} could be achieved at low rates for the former while it is 615 mAh g^{-1} for the latter. To the best of our knowledge, none of the phases of $ZnSnP_2$ have been studied as anode material for LIB.

In the present studies, chalcopyrite phase of $ZnSnP_2$ has been synthesized and used as an anode in LIB. The chalcopyrite has been found to get converted into sphalerite phase upon cycling as observed by in-situ Raman spectroscopy. The intermediate phases formed during various stages of lithiation – de-lithiation are analyzed by XRD technique. Li salt of PAA (poly acrylic acid) is used as binder along with water as the solvent for the fabrication of anode. The environmentally friendly nature of the components used in the fabrication will avoid the use of toxic solvents required for fluoro-polymer based binders. Reversible capacity of 1890 mAh g^{-1} is observed after 500 cycles at a rate of 0.3 A g^{-1}, while a reversible capacity of 750 mAh g^{-1} at a high rate of 5 A g^{-1} is observed towards the end of 1700 cycles. Good reversibility is observed when the cell is switched between high (15 A g^{-1}) and low current rates (0.1 A g^{-1}). Full cell studies using $ZnSnP_2$ anode and $LiCoO_2$ cathode reveal stable performance and with possibility of using high discharge rates. The outstanding performance of this material is compared with the recent literature on Sn-based anodes for LIB (Table S1, Supporting Information).

Results and Discussion

Material characterization

$ZnSnP_2$ crystals with chalcopyrite structure are formed in pure phase and all the experimentally obtained XRD peaks could be indexed to the standard pattern (JCPDS 01-073-0396) as shown in Figure 1(a). It crystallizes in tetragonal crystal system with space group I$\bar{4}$2d, $a = 5.651$ Å, $c = 2a = 11.302$ Å. The high intensity reflections are indexed accordingly. The peak at $2\theta = 27.3°$ corresponds to (112) reflection with an interplanar distance of 3.3 Å and has the highest intensity. Along with (112), the diffraction peaks of (204) and (312) are sharp and intense indicating the highly crystalline nature of the material. Rietveld refinement technique is used to refine the XRD data as shown in Figure S1. It shows that the experimental and calculated patterns match well and indicates the crystalline phase of chalcopyrite $ZnSnP_2$. The crystalline structure of chalcopyrite phase $ZnSnP_2$ is obtained using CIF files and material studio software (Figure 1b). It consists of unit cells in which each cation (zinc/tin) is tetrahedrally bonded to different anions (phosphorous) and is free from any tetragonal distortion. Bright field TEM image of $ZnSnP_2$ crystal is shown in Figure 1(c) along with the high-resolution TEM (HRTEM) image
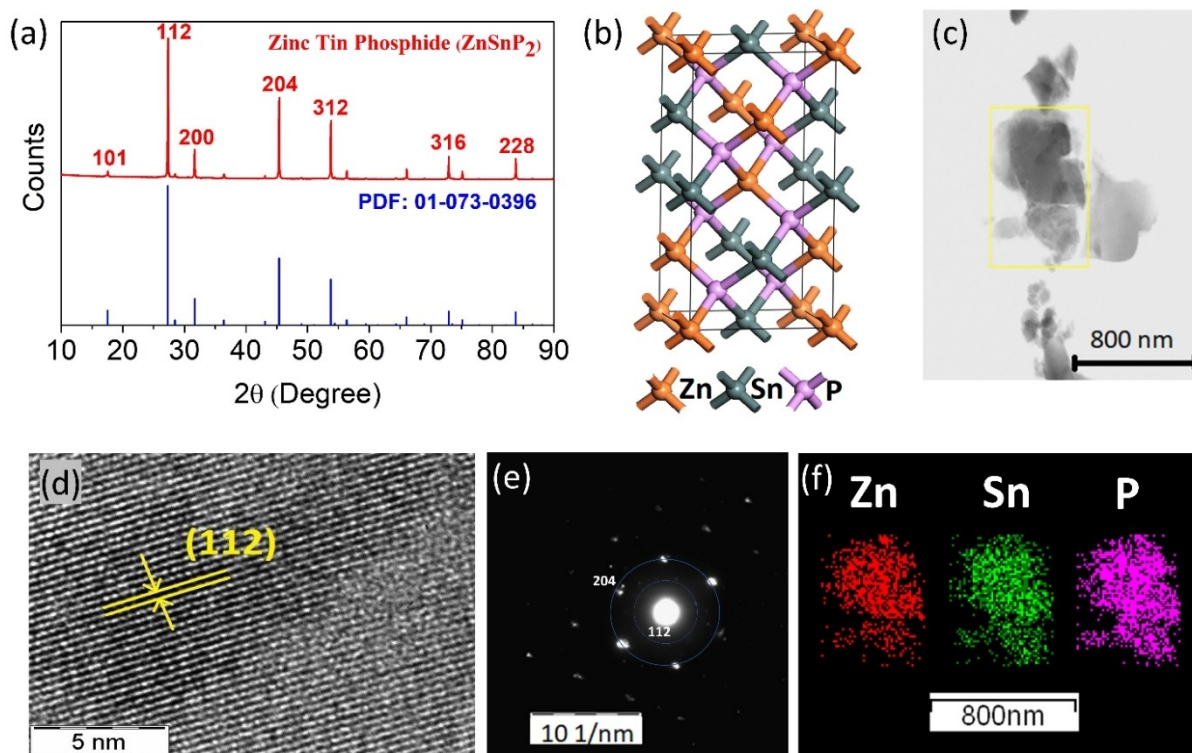

Figure 1. a) XRD pattern of chalcopyrite phase $ZnSnP_2$ crystals formed by flux method (reference pattern is also given); b) ball and stick model of $ZnSnP_2$ unit cell; c) bright field TEM image of $ZnSnP_2$ crystal; d) HRTEM image with d-spacing of 3.3 Å corresponding to the (112) reflection; e) SAED pattern; f) elemental mapping of Zn, Sn, and P.

(Figure 1d). It clearly reveals the lattice fringes indicating a crystalline phase with a d-spacing of 3.3 Å corresponding to (112) lattice plane. The bright spots in the SAED pattern imply its highly crystalline nature with tetragonal symmetry and crystal planes of (204) and (112) for the chalcopyrite $ZnSnP_2$ phase are clearly observed in Figure 1(e). The elemental mapping and EDS analysis as shown in Figure 1(f) indicates very homogeneous distribution of Zn, Sn, and P across the $ZnSnP_2$ crystal. The morphology of the pristine material is analyzed using SEM. As shown in Figure S2, $ZnSnP_2$ crystals ranging from few microns to few hundred nanometers size distribution are observed. Further, the chemical structure and purity of the formed material is analyzed using Raman spectroscopy. The spectrum as shown in Figure 2(a) is dominated by an intense peak at 308 cm^{-1} followed by low intensity peaks at 328, 343, 358, and 363 cm^{-1}. Mintairov et al. have reported the Raman spectrum of $ZnSnP_2$ grown by using gas source molecular beam epitaxy (MBE) and the data obtained in the present study match well with that of ordered chalcopyrite phase of $ZnSnP_2$ crystal.[28] A strong peak observed around 308 cm^{-1} in the xx and $x'x'$ configurations possesses Γ_1 symmetry whereas the band around 363 cm^{-1} corresponds to Γ_{4L} symmetry. The intermediate weak bands are assigned to Γ_{5T} and Γ_{4L} modes. No peaks corresponding to possible by-products (ZnP_2/Zn_3P_2) are present.[29–31] XPS technique is used to investigate the composition where the survey spectrum (Figure S3) shows the presence of Zn, Sn and P. Zinc is present

in +2 state and the high-resolution 2p core level region (Figure 2b) exhibits spin orbit doublet peaks at 1021.8 and 1044.9 eV corresponding to Zn 2p$_{3/2}$ and Zn 2p$_{1/2}$ levels, respectively. Sn^{+4} exists in chalcopyrite $ZnSnP_2$ (Figure 2c), and its presence is confirmed by the deconvoluted peaks at 495.5 eV for Sn 3d$_{3/2}$ and 487 eV for Sn 3d$_{5/2}$ level. Etching of crystals using dilute solutions of HCl and HNO$_3$ is required to avoid surface contamination due to possible presence of SnO which may lead to both Sn^{+2} and Sn^{+4} in the high-resolution spectra of Sn 3d. The P 2p core level peak is observed at 128.8 eV (Figure 2d).

Electrochemical performance and analysis

Cyclic voltammetry studies are carried out to understand the Li storage properties of $ZnSnP_2$. The voltammograms are recorded in the range of 0.01 to 2 V at a scan rate of 0.05 mV s^{-1} (Figure 3a). During the first cathodic scan, a reduction peak starts around 0.6 V which consists of a shoulder and intensifies at around 0.25 V. This high intensity peak corresponds to the process of Li-ion uptake into the $ZnSnP_2$ crystal lattice during which the solvated Li-ions move towards the anode and enter the crystal lattice. This leads to a reductive decomposition of the electrolyte components on fresh anode surface which leads to high currents during the first cycle that corresponds to the formation of solid electrolyte interphase (SEI) on the anode
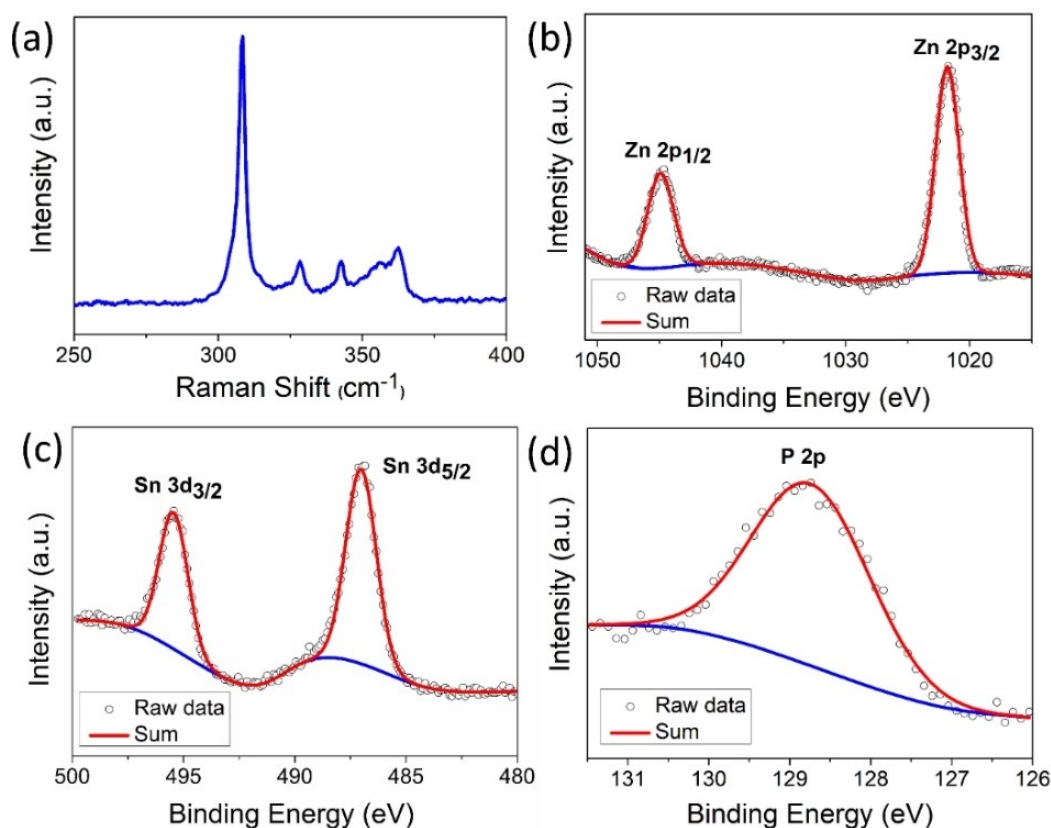

Figure 2. a) Raman spectrum of cation-ordered chalcopyrite phase $ZnSnP_2$; high resolution deconvoluted XPS spectra of b) Zn 2p, c) Sn 3d, and d) P 2p core levels. The experimental data along with fitted data are shown.
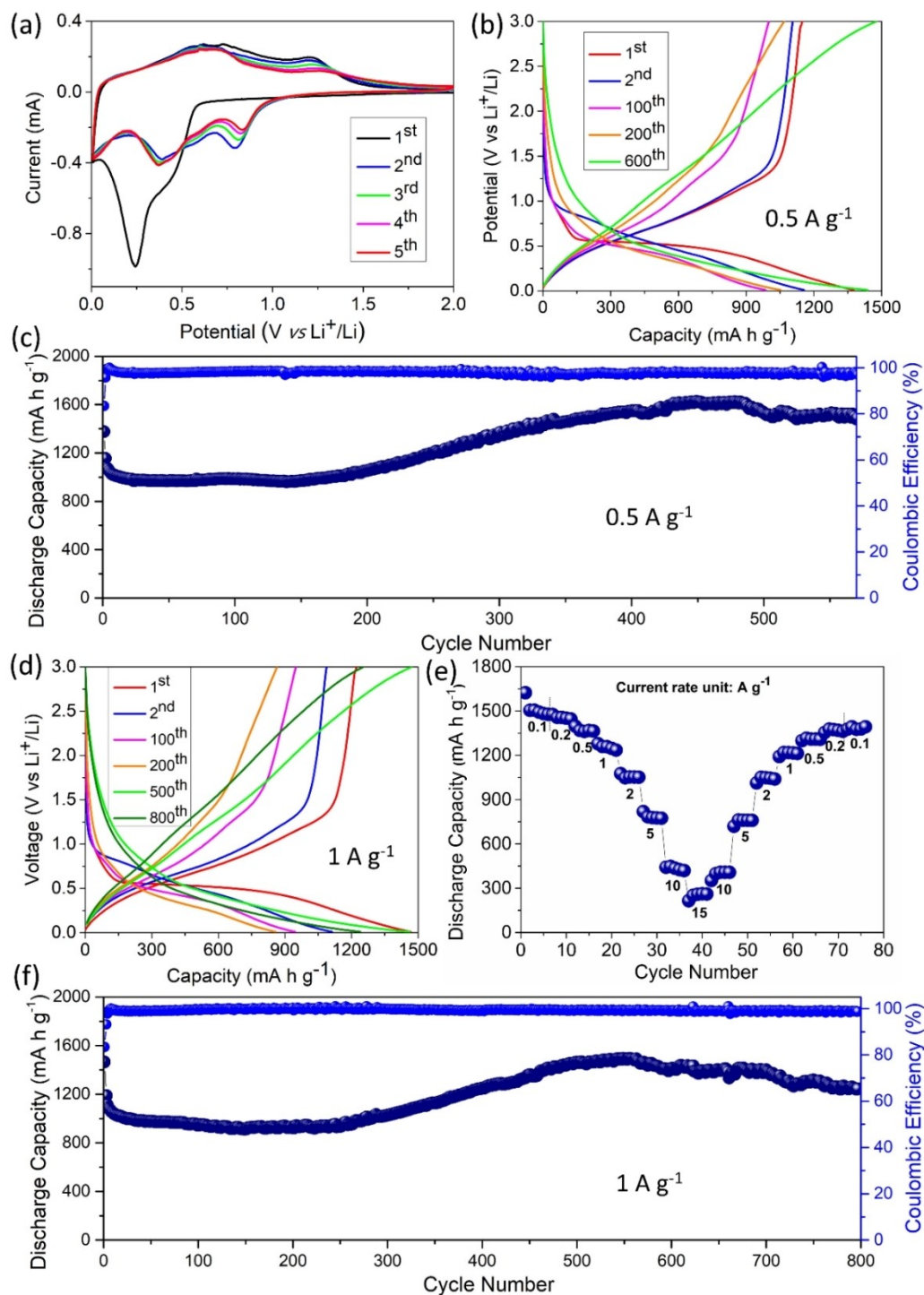
Figure 3. a) Cyclic voltammograms (first to fifth) of chalcopyrite phase ZnSnP$_2$; b) galvanostatic charge-discharge profiles at 0.5 A g^{-1} (different cycle numbers are shown) and d) at 1 A g^{-1}; c) cycling performance up to 550 cycles at a rate of 0.5 A g^{-1}, and f) up to 800 cycles at a rate of 1 A g^{-1}; e) rate performance at various current densities from 0.1 to 15 A g^{-1}.

surface. The corresponding anodic scan contains two small peaks at 0.62 and 0.73 V within a broad peak and another peak at 1.2 V. In the subsequent cathodic scans two peaks at 0.37 and 0.79 V are observed. The peak at 0.79 V shifts to higher potentials with cycling, which may be due to reduced polarization of the electrode. This may be due to the formation of defects during the phase transformation of ZnSnP$_2$ after its activation during the first cycle.[32,33] During discharge, the observed initial peak signifies Li-ion intercalation process followed by the formation of LiZnP/Li$_u$SnP$_v$ – based conversion products and the formation of Li$_x$P/Li$_y$Sn/Li$_z$Zn based intermediates towards the end of the discharge. The crystalline

intermediates discussed above are found to be formed at various stages of cycling as analyzed by ex-situ XRD of the electrodes and will be discussed later. In the subsequent anodic scans, a sharp increase in current observed from 0.01 to 0.5 V signifies Li-ion extraction from Li alloy-based intermediates such as $Li_xP/Li_ySn/Li_zZn$, whereas the oxidation humps centered at around 0.67 and 1.2 V resemble Li-ion extraction from LiZnP/Li_uSnP_v intermediates and its deintercalation to re-form $ZnSnP_2$.[34–37]

Charge-discharge curves are recorded by cycling the cells in the potential range of 0.01 to 3 V vs. Li^+/Li. The potential window is chosen to exploit the Li storage properties of the anode material to full extent. The capacity contributions in different potential windows are also studied and presented in the supporting information (Figure S4). For a potential window of 0.01–3 V, a capacity of 1300 mAh g^{-1} is observed at a rate of 0.2 A g^{-1} in the initial cycles, whereas the capacity drops to around 500 mAh g^{-1} when the potential window used is from 0.5 to 3 V. Good reversibility of discharge capacities are observed when the potential windows are switched. First discharge of the half cells is carried out at one-fourth of the actual rate to ensure complete formation of SEI on the anode surface, which helps in achieving stable capacities in subsequent cycles. The cells are cycled at various rates such as 0.2, 0.5, 1, and 2 A g^{-1}. The capacities are found to decrease up to few tens of cycles after which the values become constant and slowly start to increase around 150 cycles in all the cases. The increase in capacity is pronounced at low rates. For a rate of 0.5 A g^{-1}, first discharge is carried out at 0.12 A g^{-1} and capacity of 1375 mAh g^{-1} is obtained. Further, a reversible capacity of around 970 mAh g^{-1} is observed in the initial cycles after which it starts to increase and reaches a peak of 1626 mAh g^{-1} around 460 cycles followed by a slow decay of capacity to 1437 mAh g^{-1} (Figure 3b, c). Interestingly, a similar behavior is observed at high current rates such as 1 A g^{-1} where, initially the capacity stabilizes around 912 mAh g^{-1} at the end of 150 cycles and thereafter increases to 1495 mAh g^{-1} at around 550 cycles followed by a capacity of 1245 mAh g^{-1} towards the end of 800 cycles (Figure 3d, f). The performance for other rates such as 0.3 and 5 A g^{-1} are shown in Figures S5 and S6. Use of only acetylene black as an active material under identical conditions yields an approximate capacity of around 160 mAh g^{-1} at a rate of 0.5 A g^{-1} (Figure S7) and it decreases as a function of discharge current rate.

The increase in capacity may be due to phase conversion from chalcopyrite to sphalerite phase as the latter one offers much less resistance as compared to the former in terms of band gap and also due to the symmetric nature of the cubic phase. During the initial stages of charge-discharge, the chalcopyrite phase slowly converts to sphalerite with cycling. The poor performance of the ordered phase is predicted to be balanced by the superior performance of the disordered phase, which results in stable capacities up to 200 cycles in most cases. When the fraction of disordered phase exceeds that of the ordered phase, the capacity starts to increase continuously and reaches a maximum signifying complete transformation. After this stage, capacity almost becomes constant. As a result

of continuous cycling, a small decrease due to an increased cell resistance is observed. Further, cyclic voltammetry studies are carried out at different stages of cycling to understand the enhanced capacity behavior of $ZnSnP_2$ after certain number of cycles (Figure S8). The peak currents are found to increase as a function of number of cycles and scan rate, which indicates a possible increase in capacitive contribution with cycling. As shown in Figure S9, the capacitive contribution is observed to increase with scan rate. During the initial stages, before cycling, an increase in capacitive contribution from 81 % to 91 % is observed for an increase in scan rate from 0.1 to 0.6 mV s^{-1} (Figure S9a–d). After 50 cycles, the capacitive contribution increases to 90 % and 96 % for a scan rate of 0.1 and 0.6 mV s^{-1} (Figure S9e–h). Figure S9i represents the comparison of capacitive contribution for different scan rates at different stage of cycling. This is supported by electrochemical impedance spectroscopy as explained later. Rate capability studies (Figure 3e) are carried out by charging – discharging the cell at variable current densities from 0.1 to 15 A g^{-1}. A good reversibility in discharge capacities is observed on reversing from high to low discharge rates. It should be noted that high currents can be drawn if rate capability is carried out after full activation of the anode material. Further, a prototype full cell is assembled using $ZnSnP_2$ as anode material and $LiCoO_2$ (LCO) as the cathode material. The cell is cycled between 1 and 4 V and cycling performance is observed at a rate of 0.5 A g^{-1} as shown in Figure 4(a). A stable capacity of around 502 mAh g^{-1} is observed at the end of 170 cycles. Rate capability studies on LCO full cells indicate good reversibility after switching from extremely high current rates such as 15 A g^{-1} revealing good performance of the cell (Figure 4b).

In-situ Raman spectroscopy is carried out to understand the composition and phase change of $ZnSnP_2$ during the lithiation and de-lithiation cycles (Figure 5). All the measurements are carried out using a stainless-steel cell with a 1 mm thick quartz window as shown in Figure S10(a). The electrode to be probed is kept at the bottom with the electrode material facing upwards, which is followed by a glass fiber separator containing the electrolyte and the Li foil counter electrode is placed on top. The separator and Li foil had a hole of size < 2 mm which allows the laser to pass through and focus on the working electrode. The contacts are given using stainless-steel foil clips. The cell is assembled inside the glove box and is equilibrated for 2 h. to allow sufficient wetting in order to observe the changes in-situ. The cell is subjected to galvanostatic discharge and charge cycling between 3 and 0.01 V at a current density of 0.35 mA cm^{-2}. Raman spectra recorded during various stages of the first discharge are shown in Figure 5(a). A spectrum similar to pristine material is obtained at the open circuit conditions. In addition to the material peaks, relatively low intense peaks are observed around 470 and 525 cm^{-1}. The peak at 470 cm^{-1} may be ascribed to the deformation vibrations of SEI components[38] while the peak at 525 cm^{-1} is due to the electrolyte.[39] The presence of electrolyte peak in all the spectra confirms its presence in the area being analyzed, which is important to observe any potential dependent changes occurring on the electrode surface. The peak at 470 cm^{-1} slowly
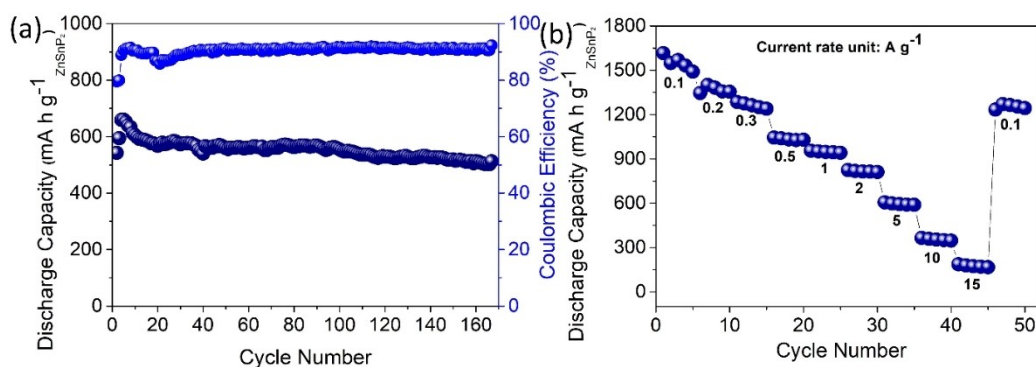
Batteries & Supercaps

Research Article
doi.org/10.1002/batt.202200132

Chemistry Europe
European Chemical
Societies Publishing

Figure 4. Full cell performance of LIB employing $ZnSnP_2$ as anode and $LiCoO_2$ as cathode material, a) cycling performance at a rate of 0.5 A g^{-1}; b) rate capability at various rates from 0.1 to 15 A g^{-1}.
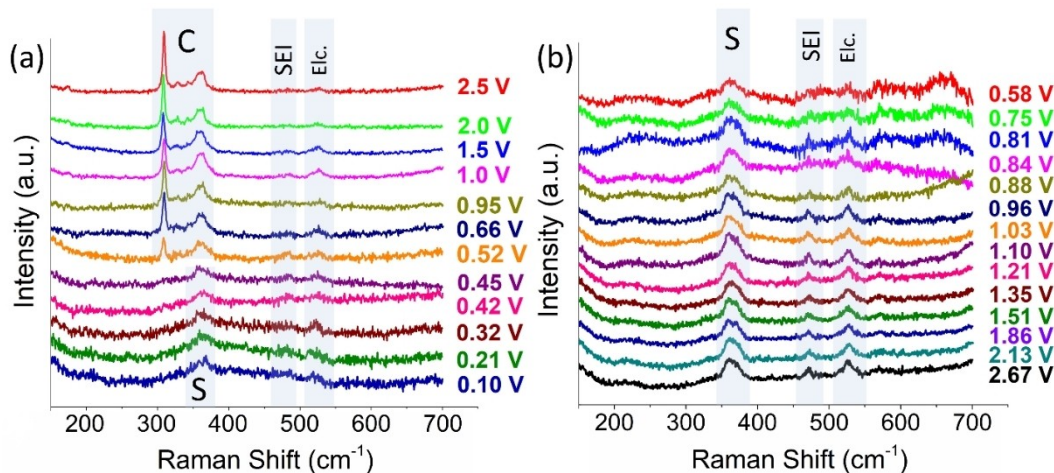

Figure 5. In-situ Raman spectra of $ZnSnP_2$ anode electrode as a function of voltage, a) discharge b) charge. C, S, SEI, Elc denote chalcopyrite, sphalerite, SEI components, electrolyte components, respectively.

gains in intensity as the discharge proceeds and becomes significantly intense towards the end of first charge due to the formation of SEI components during the cycling. The high intensity peak of $ZnSnP_2$ at 308 cm^{-1} slowly becomes less intense with decreasing potential as the first discharge proceeds and disappears at around 0.45 V. The broad peak at around 359 cm^{-1} may be assigned to the longitudinal optical (LO) phonon mode of $ZnSnP_2$ and it slowly becomes the dominant band at the end of discharge. This observation suggests a possible transformation of $ZnSnP_2$ to a disordered state.[28] During the charging process, the band at 359 cm^{-1} slowly gains in intensity with increasing potential and is the only dominant band representative of the $ZnSnP_2$ anode at the end of charge (Figure 5b). Raman spectra for lower potentials during the charging process is shown in Figure S10(b). The characteristic peaks of the ordered chalcopyrite at 308, 328, and 343 cm^{-1} do not re-appear during the charging process as the lithium ions are released from the anode. This suggests a permanent phase change of $ZnSnP_2$ anode to the disordered sphalerite phase. It should be noted that the cation-disordered phase helps in achieving better cycling than that of the ordered chalcopyrite phase due to enhanced stress accommodation

based on higher symmetry than the corresponding ordered phase.[40,41] This type of order-disorder transition induced by external factors has been briefly studied in the literature for various crystals. Pressure based transition from chalcopyrite to sphalerite phase have been reported for $ZnSnP_2$ and $ZnGeP_2$.[42] Temperature dependent transitions have been studied for $ZnSnP_2$, where annealing the crystals at 600 °C under vacuum conditions results in the rearrangement of cations within the structure leading to a phase transformation from sphalerite to chalcopyrite phase.[43] Electrochemical conversion of SnO_2 anode for Li-ion battery from tetragonal phase to cubic Sn has been reported after first thousand lithiation-de-lithiation cycles.[44] Similarly, phase conversion in antimony based anode materials has been attributed to the intermediate phases such as Li_3Sb, where cubic phase of starting material is formed upon displacement of Li by Zn and Sn.[27]

Further, the morphology of the electrode is followed using SEM. The pristine electrode contains particles of few micrometers size distributed evenly over the analyzed area (Figure S11a). The morphology changes upon cycling the electrode (100 cycles) at a rate of 0.2 A g^{-1} reveals that the particles as observed in pristine electrode get converted to irregular shapes

Batteries & Supercaps

Research Article
doi.org/10.1002/batt.202200132

Chemistry
Europe

European Chemical
Societies Publishing

as a result of various electrochemical reactions that happen during the charge and discharge processes (Figure S11b–d). The surface area of the electrode material after cycling is observed to be higher than that of pristine electrode, which may also have contributed towards improved performance with the cycling.

Ex-situ XRD has been carried out at various stages of lithiation and de-lithiation to understand the changes occurring on the electrode. The XRD pattern for pristine electrode is also given for comparative purpose (Figure S12a). When the cell is discharged to 0.45 V, all the characteristic peaks of $ZnSnP_2$ are found to be shifted to low two theta values (Figure S12b). Also, the intensities of the peaks start to decrease as the cell is discharged to low potentials. Low intensity peaks corresponding to different intermediates such as LiZnP, Li_8SnP_4, and Li_5SnP_3 are observed at a cell potential of 0.25 V (Figure S12c), which indicates the transformation of $ZnSnP_2$ anode at the conversion stage. On further discharging the cell to 0.01 V, some of the intermediate peaks observed earlier disappear and new low intense peaks corresponding to LiZn, Li_3P and $Li_{13}Sn_5$ appear. When the potential increases due to charging, extremely low intense peaks corresponding to LiZnP, Li_8SnP_4, and Li_5SnP_3 re-appear up to a potential of 0.9 V followed by the $ZnSnP_2$ peaks towards the end of charging. It should be noted that the scan rate used for recording the x ray diffractograms is very low. A long scan of around 10 h. is required to observe changes on the electrode surface. The intensities corresponding to $ZnSnP_2$ and the intermediates are weak possibly due to low crystallinity of species caused by Li insertion and extraction. It is observed (Figure S12) that the presence of cubic phase intermediates mentioned above may be responsible for the phase conversion of tetragonal to cubic phase $ZnSnP_2$. Based upon the intermediates observed in ex-situ XRD, a possible mechanism is suggested (Scheme 1, supporting information) indicating various electrochemical reactions happening during charge and discharge processes.

Electrochemical impedance spectroscopy (EIS) is carried out to understand the mechanistic details and to study the interfacial changes due to chemical transformations upon cycling. Figure S13 shows the impedance data in the form of Nyquist plots obtained at various stages of charge – discharge cycling. The experimental data collected at a potential of 1.8 V vs. Li^+/Li are fitted based on the equivalent circuit as shown in the inset. R_s represents the solution resistance which has contributions from the electrolyte soaked in glass fiber separator. R_{SEI} represents the resistance due to the SEI film formed on the electrode surface and CPE 1 corresponds to constant phase element. R_{CT} represents the charge transfer resistance along with its CPE 2. The diffusion of Li ions across the solid-liquid interface is represented by Warburg impedance (W_R). The high frequency intercept of around 5 Ω on the real Z axis is same for all the studies except for the one at 1000 cycles, for which an intercept of 10 Ω is observed. A constant intercept indicates that the ionic resistance of the electrolyte and the contact resistance between the material and current collector do not change for at least 500 cycles after which the R_s increases indicating possible electrolyte depletion or erosion of

electrode material from the copper current collector. The diameter of the semicircle corresponding to the intermediate frequency region represents the R_{ct}. The R_{ct} decreases drastically after the first cycle due to easy Li ion movement across a more ordered sphalerite structure as compared to the chalcopyrite structure. With cycling, the R_{ct} further reduces up to 100 cycles and becomes constant thereafter up to 500 cycles due to increased active surface area of the electrode, which facilitates improved Li ion insertion and extraction across the electrode material. On further cycling, an increase in the R_{ct} is observed (upto the end of 1000 cycles) indicating possible degradation of the interface material. The low frequency region represents a straight line and corresponds to diffusion of Li ions across the electrode-electrolyte interface. The slope of the line increases with cycling and reaches a maximum at around 500 cycles indicating low diffusive and high capacitive contribution leading to a good performance as compared to initial cycles.

The cycling performance of $ZnSnP_2$ anode can be enhanced by low-rate cycling during initial stages. As shown in Figure S6, the cell displays very stable performance at a rate of 5 A g^{-1} for extended cycles after it is cycled initially at 0.2 A g^{-1} rate up to 330 cycles. The low-current cycling helps in conditioning the surface probably forming a stable SEI layer which is important for the long cycle life of LIB. It prevents electrolyte decomposition on the anode surface where drastic volume changes happen during cycling. Application of very high currents from initial stages lead to the formation of improper SEI and in turn paves the way for its continuous reformation at the cost of electrolyte components. The high-capacity contribution from $ZnSnP_2$ anode could be due to the conversion nature of the material. It should be pointed out that the sphalerite phase is consistently observed as a function of cycling (Figure S14) until the conversion products start to dominate.

Conclusion

In summary, conversion of chalcopyrite phase $ZnSnP_2$ to sphalerite phase leads to improved performance with high-rate capability. The chalcopyrite synthesized by flux method shows fairly high capacities of around 1800 mAh g^{-1} at 0.3 A g^{-1}, 1626 mAh g^{-1} at 0.5 A g^{-1}, 1495 mAh g^{-1} at 1 A g^{-1}, and 1202 mAh g^{-1} at 2 A g^{-1}. In-situ Raman studies help in understanding the conversion of ordered chalcopyrite phase with tetragonal structure into disordered sphalerite phase having cubic structure upon cycling. The cation-disordered phase being symmetric helps in obtaining good reversibility during charge discharge cycling and long cycle life. Ex-situ XRD measurements at various stages of lithiation and de-lithiation indicates the formation of various Li based intermediates and subsequently shows the re-appearance of $ZnSnP_2$ towards the end of first cycle. The conversion reactions that occur during charge – discharge processes help in achieving high capacity. Reducing the size of $ZnSnP_2$ crystals may help in achieving better performance. Composites of the anode material may improve the electronic conductivity, in turn show good electrochemical characteristics.

Batteries & Supercaps

Research Article
doi.org/10.1002/batt.202200132

Chemistry
Europe

European Chemical
Societies Publishing

Experimental Section

Synthesis of ZnSnP2 and characterization

$ZnSnP_2$ can be synthesized only by a few limited techniques such as epitaxial growth, flux technique and trioctylphosphine (TOP)-based solution growth.[45,46] Pure phase (chalcopyrite or sphalerite) of the material can be obtained by epitaxial growth in the form of thin films on suitable substrates but obtaining bulk material becomes difficult using this technique. On the other hand, TOP-based synthesis results in the formation of mixed phases of $ZnSnP_2$ and limits the scope of further studies due to the difference in structural and electronic properties of the two phases. Flux technique is quite successful for the synthesis of pure phase chalcopyrite $ZnSnP_2$ by slow cooling. Fast cooling leads to the formation of mixed phases and it becomes difficult to obtain pure sphalerite phase.

In the present study, $ZnSnP_2$ crystals were synthesized by using a flux method from a 92 mol% solution of Sn.[47] The elements, Zn powder (99.9% Alfa Aesar), Sn powder (99.99% Sigma Aldrich), red phosphorous powder (99.9% Alfa Aesar) were sealed in their stoichiometric ratio in an evacuated quartz tube at a pressure of 10^{-6} mbar. The tube was suspended in a vertical furnace and maintained at 700°C for 24 h. for homogenization. The sample tube was then lowered at a rate of 1.3 mm per hour. in order to solidify the solution from the bottom. Excess Sn in the formed ingot was dissolved using 0.1 M HCl solution and grey colored crystals of $ZnSnP_2$ were obtained. The crystals were ground to fine powder and characterized using PANalytical X-Ray diffractometer with Cu K_α (1.5418 Å) as the X-ray source. Raman spectra were recorded using 514.5 nm laser source on a LabRAM HR, Horiba Jobin Yvon, France spectrometer. In-situ measurements were carried out on customized stainless-steel cell with a 1 mm thick quartz window. The power of Raman laser was maintained in a range of 1.5 to 1.7 mW for all the studies. The surface morphology was analyzed using scanning electron microscopy (SEM) (Carl Zeiss Ultra 55). Transmission electron microscopy (TEM) analysis was carried out on a JEOL 2100 F microscope at an acceleration voltage of 200 kV.

Electrochemical measurements

Li–PAA was used as a binder for the current study. It was prepared by neutralizing 5 wt% aqueous solution of poly(acrylic acid) (PAA, $M_w = 450,000$, Sigma-Aldrich) with lithium hydroxide (LiOH). $ZnSnP_2$ was ground with acetylene black carbon along with Li–PAA binder in the ratio of 7:2:1 and the obtained slurry was coated on a circular copper foil with 12 mm diameter. The electrodes were dried at 60°C in a vacuum oven for 12 h. The loading was maintained in the range of 0.8 to 1 mg cm^{-2} for half cells. Electrochemical testing was carried out using CR 2032 type coin cells which were assembled inside an argon filled glove box with O_2 and H_2O concentration less than 0.1 ppm. Whatman glass fiber was used as a separator. The electrolyte used was 1 M lithium hexafluorophosphate (LiPF$_6$) in ethylene carbonate (EC) and diethyl carbonate (DEC) (1:1 v/v) with 5 wt% fluoroethylene carbonate (FEC) as an additive. The electrolyte quantity was optimized to be 90 μL for all the studies. Lithium foil (0.75 mm thick, Aldrich) was used as a counter electrode for half-cell studies and LiCoO$_2$ (Aldrich) was used as a cathode for full cell studies. For LiCoO$_2$/ ZnSnP$_2$ full cells, cathode to anode capacity balancing ratio was optimized to be 1.3:1. This ratio was used considering an approximate capacity of LiCoO$_2$ as 160 mAh g^{-1} and 1300 mAh g^{-1} for ZnSnP$_2$. The full cell capacity was limited by ZnSnP$_2$ anode. The ZnSnP$_2$ anode used for full cell was pre-lithiated by slowly

discharging a half-cell at a rate of 0.1 A g^{-1}. The recovered lithiated-electrode was then used as anode for the fabrication of full cell. The cells were stabilized for 4 h. at rest before the electrochemical studies were carried out. Cyclic voltammetry (CV) studies and EIS measurements were carried out on Autolab (PGSTAT30) electro-chemical workstation. The impedance measurements were re-corded in the frequency range from 100 kHz to 0.1 Hz with an ac amplitude of 10 mV peak to peak. The data were analyzed using Zsimpwin software. Galvanostatic cycling of ZnSnP$_2$ half cells and LiCoO$_2$/ZnSnP$_2$ full cells were performed under ambient conditions (25 C) using Arbin instrument (MSTAT) and data analysis was carried out using MITS-Pro (version 4.24) software.

Conflict of Interest

The authors declare no conflict of interest.

Data Availability Statement

The data that support the findings of this study are available in the supplementary material of this article.

[1] G. E. Blomgren, *J. Electrochem. Soc.* **2017**, *164*, A5019–A5025.
[2] Y. Yamada, Y. Iriyama, T. Abe, Z. Ogumi, *Langmuir* **2009**, *25*, 12766–12770.
[3] K. H. Chen, M. J. Namkoong, V. Goel, C. Yang, S. Kazemiabnavi, S. M. Mortuza, E. Kazyak, J. Mazumder, K. Thornton, J. Sakamoto, N. P. Dasgupta, *J. Power Sources* **2020**, *471*, 228475.
[4] J. Billaud, F. Bouville, T. Magrini, C. Villevieille, A. R. Studart, *Nat. Energy* **2016**, *1*, 1–6.
[5] O. Chernysh, V. Khomenko, I. Makyeyeva, V. Barsukov, in *Materials Today: Proceedings*, Vol.6, **2019**, pp. 42–47.
[6] J. Asenbauer, T. Eisenmann, M. Kuenzel, A. Kazzazi, Z. Chen, D. Bresser, *Sustain. Energy Fuels* **2020**, *4*, 5387–5416.
[7] L. J. Hardwick, M. Marcinek, L. Beer, J. B. Kerr, R. Kostecki, *J. Electrochem. Soc.* **2008**, *155*, A442.
[8] S. Das, M. Z. Bazant, *ECS Meeting Abstract* **2020**, *MA2020-02*, 110.
[9] S. Klein, P. Bärmann, T. Beuse, K. Borzutzki, J. E. Frerichs, J. Kasnat-scheew, M. Winter, T. Placke, *ChemSusChem* **2021**, *14*, 595–613.
[10] H. Tian, F. Xin, X. Wang, W. He, W. Han, *J. Materiomics* **2015**, *1*, 153–169.
[11] L. F. Cui, Y. Yang, C. M. Hsu, C. Yi, *Nano Lett.* **2009**, *9*, 3370–3374.
[12] X. Li, A. M. Colclasure, D. P. Finegan, D. Ren, Y. Shi, X. Feng, L. Cao, Y. Yang, K. Smith, *Electrochim. Acta* **2019**, *297*, 1109–1120.
[13] I. T. Lucas, E. Pollak, R. Kostecki, *Electrochem. Commun.* **2009**, *11*, 2157–2160.
[14] G. Kim, S. Jeong, J. H. Shin, J. Cho, H. Lee, *ACS Nano* **2014**, *8*, 1907–1912.
[15] C. Liang, M. Gao, H. Pan, Y. Liu, M. Yan, *J. Alloys Compd.* **2013**, *575*, 246–256.
[16] G. Bree, H. Geaney, K. Stokes, K. M. Ryan, *J. Phys. Chem. C* **2018**, *122*, 20090–20098.
[17] P. Nithyadharseni, M. V. Reddy, B. Nalini, M. Kalpana, B. V. R. Chowdari, *Electrochim. Acta* **2015**, *161*, 261–268.

Batteries & Supercaps

Research Article
doi.org/10.1002/batt.202200132

Chemistry Europe
European Chemical
Societies Publishing

[18] T. Chen, R. Li, J. Liu, D. Mu, S. Sun, L. Zhao, S. Tian, W. Zhu, X. Wang, C. Dai, *J. Electroanal. Chem.* **2021**, *880*, 114847.

[19] X. Lu, F. Luo, Y. Ji, W. Zhang, Q. Tian, Z. Sui, L. Yang, *J. Alloys Compd.* **2021**, *863*, 158743.

[20] C. H. L. Goodman, *Nature* **1957**, *179*, 828–829.

[21] S. Nakatsuka, Y. Nose, T. Uda, *Thin Solid Films* **2015**, *589*, 66–71.

[22] S. Nakatsuka, S. Akari, J. Chantana, T. Minemoto, Y. Nose, *ACS Appl. Mater. Interfaces* **2017**, *9*, 33827–33832.

[23] N. Yuzawa, J. Chantana, S. Nakatsuka, Y. Nose, T. Minemoto, *Curr. Appl. Phys.* **2017**, *17*, 557–564.

[24] S. Akari, J. Chantana, S. Nakatsuka, Y. Nose, T. Minemoto, *Sol. Energy Mater. Sol. Cells* **2018**, *174*, 412–417.

[25] W. Li, X. Li, J. Liao, B. Zhao, L. Zhang, L. Huang, G. Liu, Z. Guo, M. Liu, *Energy Environ. Sci.* **2019**, *12*, 2286–2297.

[26] J. Zhou, F. Jiang, S. Li, Z. Xu, W. Sun, X. Ji, Y. Yang, *J. Solid State Electrochem.* **2019**, *23*, 1991–2000.

[27] G. Coquil, B. Fraisse, S. Biscaglia, D. Aymé-Perrot, M. T. Sougrati, L. Monconduit, *J. Power Sources* **2019**, *441*, 227165.

[28] A. M. Mintairov, N. A. Sadchikov, *Phys. Rev. B* **1999**, *59*, 15197–15207.

[29] J. Baran, Y. A. Pasechnik, K. V. Shportko, M. Trzebiatowska-Gusowska, E. F. Venger, *J. Mol. Struct.* **2006**, *792–793*, 239–242.

[30] G. Pangilinan, R. Sooryakumar, J. Misiewicz, *Phys. Rev. B* **1991**, *44*, 2582–2588.

[31] J. Misiewicz, *J. Phys. Condens. Matter* **1989**, *1*, 9283–9299.

[32] K. Zhang, M. Park, L. Zhou, G. H. Lee, J. Shin, Z. Hu, S. L. Chou, J. Chen, Y. M. Kang, *Angew. Chem. Int. Ed.* **2016**, *55*, 12822–12826; *Angew. Chem.* **2016**, *128*, 13014–13018.

[33] K. Zhang, M. Park, L. Zhou, G. H. Lee, W. Li, Y. M. Kang, J. Chen, *Adv. Funct. Mater.* **2016**, *26*, 6728–6735.

[34] L. Wang, H. Guo, W. Wang, K. Teng, Z. Xu, C. Chen, C. Li, C. Yang, C. Hu, *Electrochim. Acta* **2016**, *211*, 499–506.

[35] M. V. V. M. Satya Kishore, U. V. Varadaraju, *J. Power Sources* **2005**, *144*, 204–207.

[36] J. Qian, D. Qiao, X. Ai, Y. Cao, H. Yang, *Chem. Commun.* **2012**, *48*, 8931–8933.

[37] Y. R. Lim, C. S. Jung, H. S. Im, K. Park, J. Park, W. I. Cho, E. H. Cha, *J. Mater. Chem. A* **2016**, *4*, 10691–10699.

[38] R. Schmitz, R. A. Müller, R. W. Schmitz, C. Schreiner, M. Kunze, A. Lex-Balducci, S. Passerini, M. Winter, *J. Power Sources* **2013**, *233*, 110–114.

[39] T. Nishi, H. Nakai, A. Kita, *J. Electrochem. Soc.* **2013**, *160*, A1785–A1788.

[40] J. Sun, H. W. Lee, M. Pasta, H. Yuan, G. Zheng, Y. Sun, Y. Li, Y. Cui, *Nat. Nanotechnol.* **2015**, *10*, 980–985.

[41] H. H. Heenen, C. Scheurer, K. Reuter, *Nano Lett.* **2017**, *17*, 3884–3888.

[42] T. Basak, M. N. Rao, S. L. Chaplot, *J. Phys. Conf. Ser.*, **2012**, *377*, 012071.

[43] S. Nakatsuka, Y. Nose, *J. Phys. Chem. C* **2017**, *121*, 1040–1046.

[44] Y. Chen, B. Song, R. M. Chen, L. Lu, J. Xue, *J. Mater. Chem. A* **2014**, *2*, 5688–5695.

[45] G. A. Davis, C. M. Wolfe, *J. Electrochem. Soc.* **1983**, *130*, 1408–1412.

[46] E. J. Sheets, R. B. Balow, W. C. Yang, E. A. Stach, R. Agrawal, *Nanoscale* **2015**, *7*, 19317–19323.

[47] S. Nakatsuka, H. Nakamoto, Y. Nose, T. Uda, Y. Shirai, *Phys. Status Solidi C* **2015**, *12*, 520–523.